



**HAL**  
open science

# Eikonal surface wave tomography with smoothing splines - Application to Southern California

Sébastien Chevrot, Maximilien Lehujeur

► **To cite this version:**

Sébastien Chevrot, Maximilien Lehujeur. Eikonal surface wave tomography with smoothing splines - Application to Southern California. *Geophysical Journal International*, 2022, 229 (3), pp.1927-1941. 10.1093/gji/ggac034 . hal-03549260

**HAL Id: hal-03549260**

**<https://hal.science/hal-03549260>**

Submitted on 25 Oct 2022

**HAL** is a multi-disciplinary open access archive for the deposit and dissemination of scientific research documents, whether they are published or not. The documents may come from teaching and research institutions in France or abroad, or from public or private research centers.

L'archive ouverte pluridisciplinaire **HAL**, est destinée au dépôt et à la diffusion de documents scientifiques de niveau recherche, publiés ou non, émanant des établissements d'enseignement et de recherche français ou étrangers, des laboratoires publics ou privés.

# Eikonal surface wave tomography with smoothing splines—application to Southern California

Sébastien Chevrot<sup>1</sup> and Maximilien Lehujeur<sup>1,2</sup>

<sup>1</sup>Observatoire Midi Pyrénées, Université Paul Sabatier, CNRS, IRD, CNES, GET, UMR 5563, Toulouse, France. E-mail: [sebastien.chevrot@get.omp.eu](mailto:sebastien.chevrot@get.omp.eu)

<sup>2</sup>GERS-GeoEND, Université Gustave Eiffel, F-44344 Bouguenais, France

Accepted 2022 January 25. Received 2021 November 29; in original form 2021 May 7

## SUMMARY

The densification of both permanent and temporary seismic networks has raised new interest in surface wave eikonal tomography from which phase velocity maps can be obtained without resolving a tomographic inverse problem. However, eikonal tomography requires to reconstruct traveltimes surfaces from a discrete number of measurements obtained at the station locations, which can be challenging. We present a new method to reconstruct these traveltimes surfaces with smoothing splines discretized in a regular 2-D Cartesian grid. We impose Neumann boundary conditions so that the phase gradients on the edges of the grid are equal to the apparent slownesses of the average plane wave along the normal direction measured by beamforming. Using the eikonal equation, phase velocity maps are then derived from the norm of the gradient of the interpolated traveltimes maps. The method is applied to Rayleigh waves recorded by the Southern California Seismic Network to derive phase velocity surfaces. Robust, stable and finely resolved phase velocity maps at 25 and 33 s period are obtained after averaging the phase velocity maps derived from the analysis of a selection of recent large ( $M_w \geq 6.5$ ) teleseismic events. The phase velocity map at 25 s mainly constrains the thickness of the Southern California crust, with results that are in excellent agreement with previous tomographic studies.

**Key words:** North America; Tomography; Crustal imaging; Seismic tomography; Surface waves and free oscillations; Wave scattering and diffraction.

## 1 INTRODUCTION

With its capacity to target a specific region and to take benefit from the densification of permanent and temporary seismic networks, regional body-wave traveltimes tomography, initiated by Aki *et al.* (1977), has become a powerful and versatile approach to map lateral variations of seismic velocities in the crust and upper mantle. However, regional surface wave tomography is more challenging, because surface waves show strong deviations from a simple plane wave arrival, both in traveltimes and amplitude, which result from multipathing and scattering effects (e.g. Wielandt 1993; Friederich *et al.* 1994; Friederich & Wielandt 1995; Kolínský *et al.* 2020). These complications rule out the use of classical asymptotic (ray-based) tomographic inversions for surface waves. In his pioneering study, Wielandt (1993) emphasized that phase velocity estimates derived from the gradient of the phase are biased. Furthermore, he demonstrated that to properly determine the structural phase velocity, it is necessary to consider the complete Helmholtz equation, which adds a correction term that involves computing the Laplacian of the amplitude field, a notoriously difficult problem.

The deployment of the Transportable Array (TA) component of the EarthScope/USArray created a strong impulse to revisit the

problem of eikonal/Helmholtz tomography with surface waves generated by earthquakes (Pollitz 2008; Pollitz & Snoko 2010; Lin & Ritzwoller 2011; Liu & Holt 2015; Jin & Gaherty 2015) or extracted from ambient seismic noise (Lin *et al.* 2009; Qiu *et al.* 2019). The common idea shared by all these studies is to track the traveltimes (and amplitude) of surface wave fronts across an array of seismic stations but they differ in their strategy to address the issues raised in Wielandt (1993). Following the approach in Friederich *et al.* (1994), early attempts used a superposition of membrane waves to represent the incoming wavefield and jointly reconstructed the phase velocity model and the complete regional wavefield using a scattering integral equation derived from the Helmholtz equation (Pollitz 2008; Pollitz & Snoko 2010). This approach provided the first detailed tomographic images of upper-mantle structures beneath western USA obtained with the TA. Soon after, Lin *et al.* (2009) demonstrated that it is possible to obtain tomographic images of comparable quality with a much simpler approach that only involves interpolating the traveltimes and amplitude measurements with splines in tension (Wessel & Bercovici 1998). Once the phase traveltimes and amplitude fields are reconstructed by interpolation, the phase velocity model can then be directly obtained from the Helmholtz equation, by computing the gradient of the traveltimes field and the Laplacian

of the amplitude field. Gradiometry is a related approach that reconstructs directly the gradient of the phase and amplitude from the spatial and temporal derivative of the wavefield (Liu & Holt 2015).

Whereas these different implementations of Helmholtz tomography have demonstrated their potential for regional-scale surface wave imaging, several studies have shown that similar results can be obtained with the eikonal equation, that is, only exploiting the phase of surface waves (Bodin & Maupin 2008; Lin *et al.* 2009; Lehujeur & Chevrot 2020b). This important result opens new perspectives for significantly improving and simplifying array-based surface wave tomographic methods (e.g. Lehujeur & Chevrot 2020a). The purpose of this paper is to present a new method to reconstruct traveltime surfaces with a smoothing spline interpolation method. The main motivation for using smoothing splines compared to splines in tension is that we no longer impose an exact fit of phase measurements. In addition, we impose physically realistic Neumann boundary conditions, which ensure that the slowness on the boundaries of the regional domain is the apparent slowness derived from array beamforming. These two ingredients allow us to get very stable and robust reconstructed traveltime surfaces, without having to resort to spatial filtering, which can degrade the resolution. As an illustration, we apply the new eikonal method in southern California, a plate boundary region with mountain ranges, active seismicity and rifting.

The paper is organized as follows. In Section 2, we recall the principles of eikonal tomography, which allows us to derive the lateral variations of phase velocities from the gradient of surface wave traveltime fields. In Section 3, we detail the procedure to extract the fundamental mode of Rayleigh waves from the seismic records and to measure the instantaneous phase of the wave front at each station. Section 4 describes how these discrete phase measurements can be interpolated with smoothing splines to reconstruct traveltime surfaces in a regional grid. From the gradient of the reconstructed traveltime surfaces, it is then straightforward to derive phase velocity maps, using the eikonal equation. The different steps of this new eikonal tomography method are illustrated by applying it to Rayleigh waves recorded by the Southern California Seismic Network. We obtain robust and finely resolved phase velocity maps of Rayleigh wave phase velocity at 25 and 33 s period. In Section 5, we compare and discuss the results of smoothing spline interpolation with those obtained with splines in tension. We also provide a preliminary interpretation of these phase velocity maps and confront them to several published tomographic studies performed in that region. Finally, we present some perspectives offered by smoothing splines for Helmholtz tomography.

## 2 HELMHOLTZ/EIKONAL TOMOGRAPHY

Let us start with a brief review of eikonal/Helmholtz tomography theory. For further details, the reader should refer to Lehujeur & Chevrot (2020b). Neglecting mode coupling which has a negligible effect at long period (e.g. Tanimoto 1990; Tromp & Dahlen 1993) the wave equation can be rewritten as the Helmholtz equation

$$s^2 = \|\nabla\mathbf{T}\|^2 - \frac{\Delta\mathbf{A}}{\omega^2\mathbf{A}}, \quad (1)$$

where  $\nabla$  is the gradient operator,  $\Delta$  the Laplacian operator,  $s$  the slowness,  $\mathbf{A}$  the amplitude and  $\mathbf{T}$  the traveltime (or phase) of the wave (e.g. Červený 2001). The amplitude term, which accounts for scattering effects, is usually not negligible compared to the gradient of the traveltime. However, by averaging a large number of phase

velocity maps obtained from wave fronts coming from different source back-azimuths, its contribution tends to cancel out (Bodin & Maupin 2008; Lehujeur & Chevrot 2020b). Therefore, isotropic phase velocity maps can be obtained from the simplified Helmholtz equation

$$s^2 = \|\nabla\mathbf{T}\|^2, \quad (2)$$

often referred to as the eikonal equation. From eq. (2), we can see that the slowness (and thus the velocity) can be directly obtained from the squared norm of the traveltime gradient. The tomographic problem can thus be reformulated as an interpolation problem to reconstruct traveltime surfaces from a discrete number of traveltime measurements obtained at the station positions.

## 3 SURFACE WAVE PHASE MEASUREMENTS WITH A REGIONAL ARRAY

We first describe the complete method to extract the fundamental mode of Rayleigh waves and measure their phase. To illustrate the different steps involved in the measurement method, we use Rayleigh waves from a selection of teleseismic events recorded by the Southern California Seismic Network (Fig. 1).

### 3.1 Data selection and preparation

We have first selected all the shallow events (hypocentral depth  $\leq 100$  km) with a magnitude larger than 6.5 at an epicentral distance of less than  $100^\circ$  from the array for the time period 2017–2020. At larger distances, measurements of fundamental-mode Rayleigh waves along the minor arc are impacted by interference with major-arc overtones of Rayleigh waves (Hariharan *et al.* 2020, 2022). From this selection, we only kept 35 events for which we were able to obtain robust traveltime measurements at 33 s period. Among those events, we observed strong multipathing effects or overtone interference at 25 s for 8 events, so that we kept only 27 events for the phase measurements at 25 s period. The stronger multipathing observed at 25 s is not surprising since at this period Rayleigh are strongly sensitive to crustal thickness which varies abruptly at plate boundaries. For events coming from the NW in particular, the propagation paths closely follow the transition from the North America continental plate to the oceanic Juan de Fuca and Pacific plates. For each event, we first extracted all the vertical component waveforms recorded by the stations of the Southern California Seismic Network. The seismograms were then deconvolved from their station response and resampled at a time step of 0.2 s.

### 3.2 Isolation of the fundamental mode

The next step consists in isolating the fundamental mode of Rayleigh waves in a narrow-frequency band. In this study, we will only present results obtained at 25 and 33 s period, but we were able to obtain robust phase velocity maps for periods between 20 and 150 s. The tomographic images obtained from the complete data set will be presented in a forthcoming publication.

Fig. 2 shows the vertical component records (black lines) of the 2019 February 01 Mexico event, filtered with a third-order Butterworth filter between 0.036 and 0.044 Hz. The fundamental-mode Rayleigh wave train is predominant, but higher modes and body waves as well as noise are still present. To get clean and robust phase measurements, we extract the fundamental mode of Rayleigh

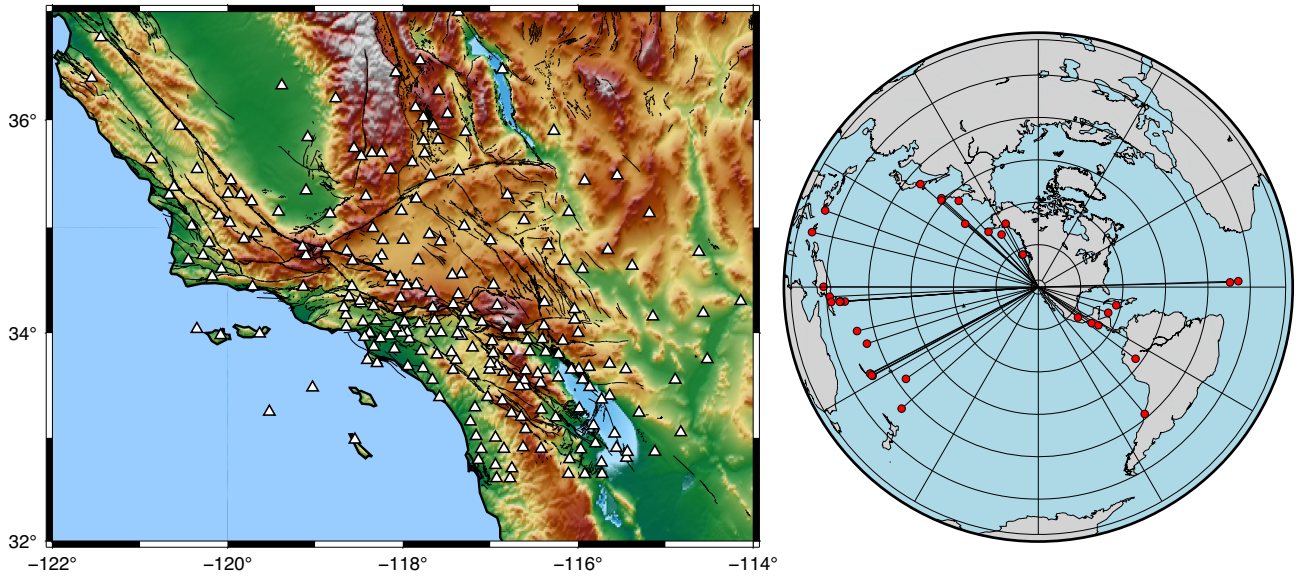


**Figure 1.** Left: map of the Southern California Seismic Network. The white triangles indicate the seismic stations available between 2017 and 2020. Right: the 35 earthquakes (red circles) selected for this study.

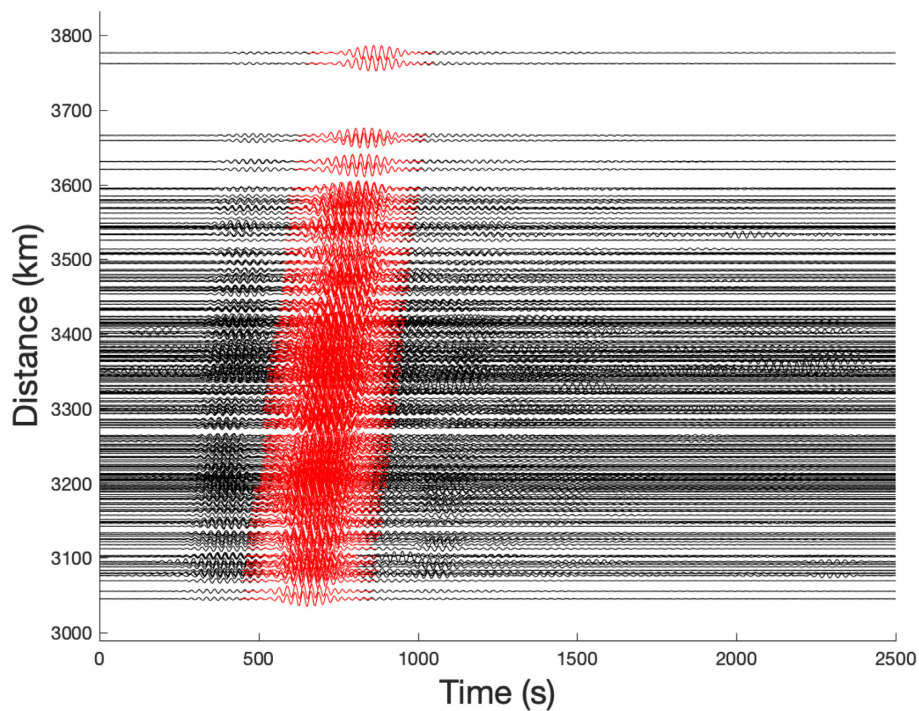


**Figure 2.** Vertical component records of the 2019 February 01 Mexico event filtered with a third-order Butterworth filter between 0.036 and 0.044 Hz (black lines). The red lines show the same traces after application of the taper that isolates the fundamental mode of Rayleigh waves.

waves, following a similar procedure as the one described in Levshin & Ritzwoller (2001), slightly modified to exploit the regional array for this extraction.

We first determine the apparent slowness and propagation direction of the wave front by beam forming, following the method described in Capon (1969). Fig. 3 shows the slowness diagram obtained from the records filtered at 0.04 Hz. This diagram is dominated by a single energetic peak that corresponds to a wave that propagates along an azimuth of  $319^\circ$  and a slowness of  $0.27 \text{ s km}^{-1}$

which corresponds to a phase velocity of  $3.7 \text{ km s}^{-1}$ . After applying a time-shift to align this main surface wave arrival at each station, we compute the envelope of the average trace, from which we determine a taper that extracts the parts of the signal that exceeds 5 per cent of the envelope maximum. This taper is applied on each individual trace after which the time-shift is removed to restore the absolute timing. In the end, the parts of the signal outside the surface wave time window have been damped (Fig. 2, red lines), which considerably reduces the impact of time interferences and noise on

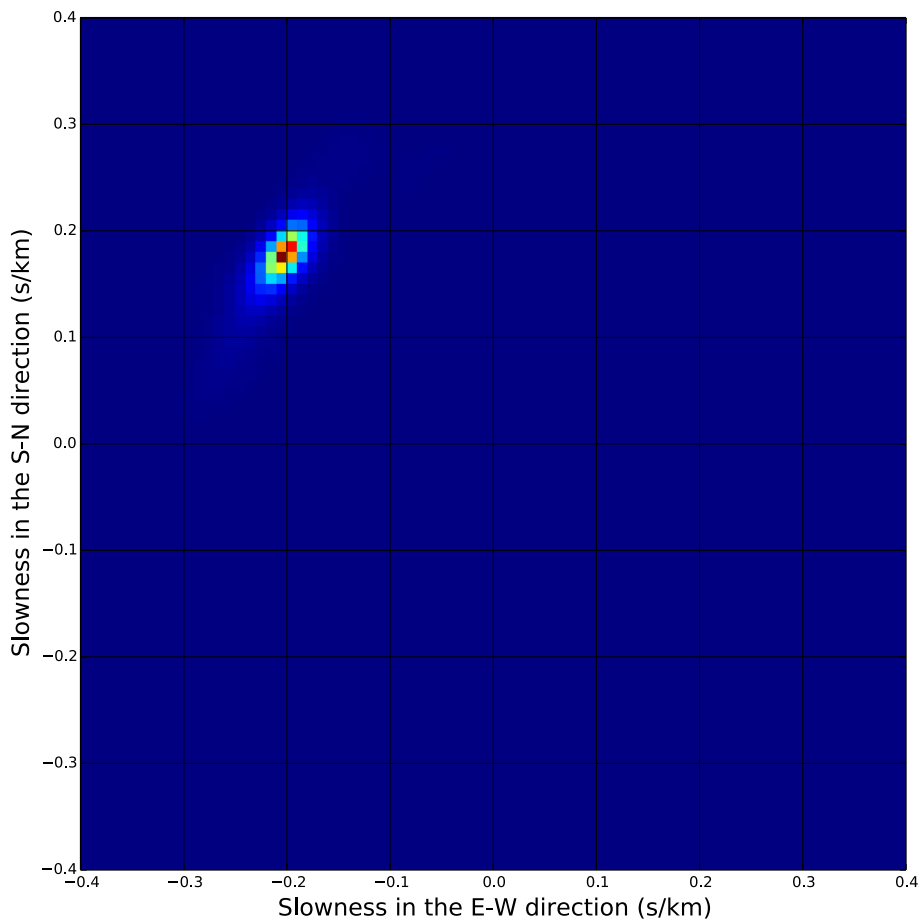


**Figure 3.** Results of the beamforming for the record section shown in Fig. 2. The main beam gives a slowness that is in good agreement with the expected slowness of a fundamental-mode Rayleigh wave. The propagation direction at  $309^\circ$  is also in very good agreement with the backazimuth of the source which is  $\sim 124^\circ$ .

phase measurements. As reported in other studies (e.g. Hariharan *et al.* 2022), we found that varying the width of the taper or the width of the bandpass filter has a negligible effect on the phase measurements.

The traveltime of the Rayleigh wave at each station is simply measured from the phase of the Fourier transform of the filtered records, divided by the angular frequency  $\omega = 2\pi f_0$ , where  $f_0$  is the analysed frequency. As a quality check, we compute the phase residuals at each station by subtracting the phase traveltime of the plane wave obtained by beamforming. This allows us to detect easily and remove the phase (and amplitude) outliers. Fig. 4 illustrates our data selection procedure on the Mexico event filtered at 25 s. The phase residuals show a spatially coherent and smooth pattern except at a few stations where they deviate by several seconds with respect to adjacent stations (Fig. 4a). In eikonal tomography, because we determine the phase velocity map from the gradient of the traveltime surface it is crucial to remove such outliers. Automatic selection criteria based upon deviations from a local median of phase residuals are difficult to apply owing to the uneven station distribution and spatial variability of the wavefields coming from different azimuths. We thus developed a simple graphical interface to visualize the phase residuals and reject the outliers manually. Fig. 4(b) shows the phase measurements for the Mexico event that were kept after visual inspection. All the other events that were selected for this study were of similar quality. Events that showed

clear interference patterns, resulting from either multipathing or interference with overtones were rejected.

### 3.1 Phase unwrapping

To correct for cycle skipping effects, we follow the approach described in Chevrot & Zhao (2007). The phase measurements are first sorted as a function of increasing epicentral distances. Because the distance between two consecutive stations is small, typically a fraction of the signal wavelength, the phase difference measured between these two stations is expected to be much smaller than the period considered. Thus, any cycle skip is easily detected and corrected for. We unwrap the phase starting from the station closest to the source, successively adding the corrected phase difference between consecutive station pairs. The unwrapped phase measurements are then visually inspected in order to discard any remaining outlier that may come for example from clock problems. The phase measurements are then simply converted to traveltimes by dividing by the angular frequency. Hereafter, whenever we will employ the term ‘phase’ it will actually design the traveltime of the wave front. Fig. 5 shows the cleaned unwrapped phase for the Mexico event at 25 s period.

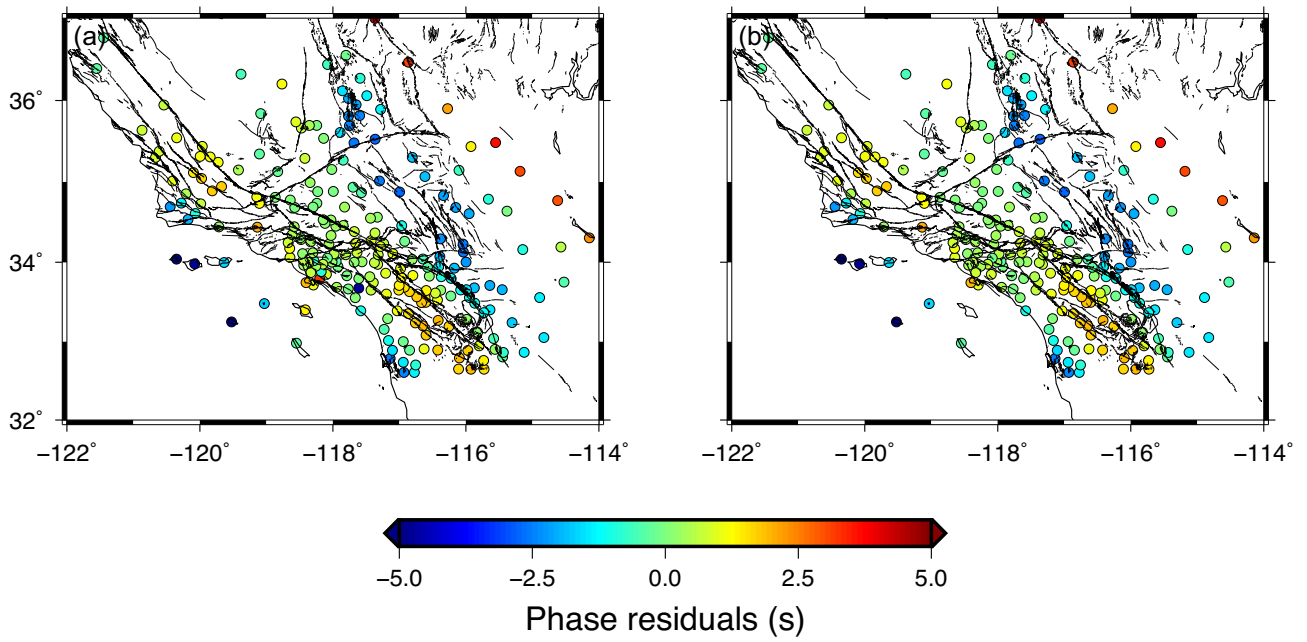


Figure 4. (a) Phase residuals (deviations from the average plane wave) for the Mexico event shown in Fig. 2. (b) Same phase residuals after removing outliers.

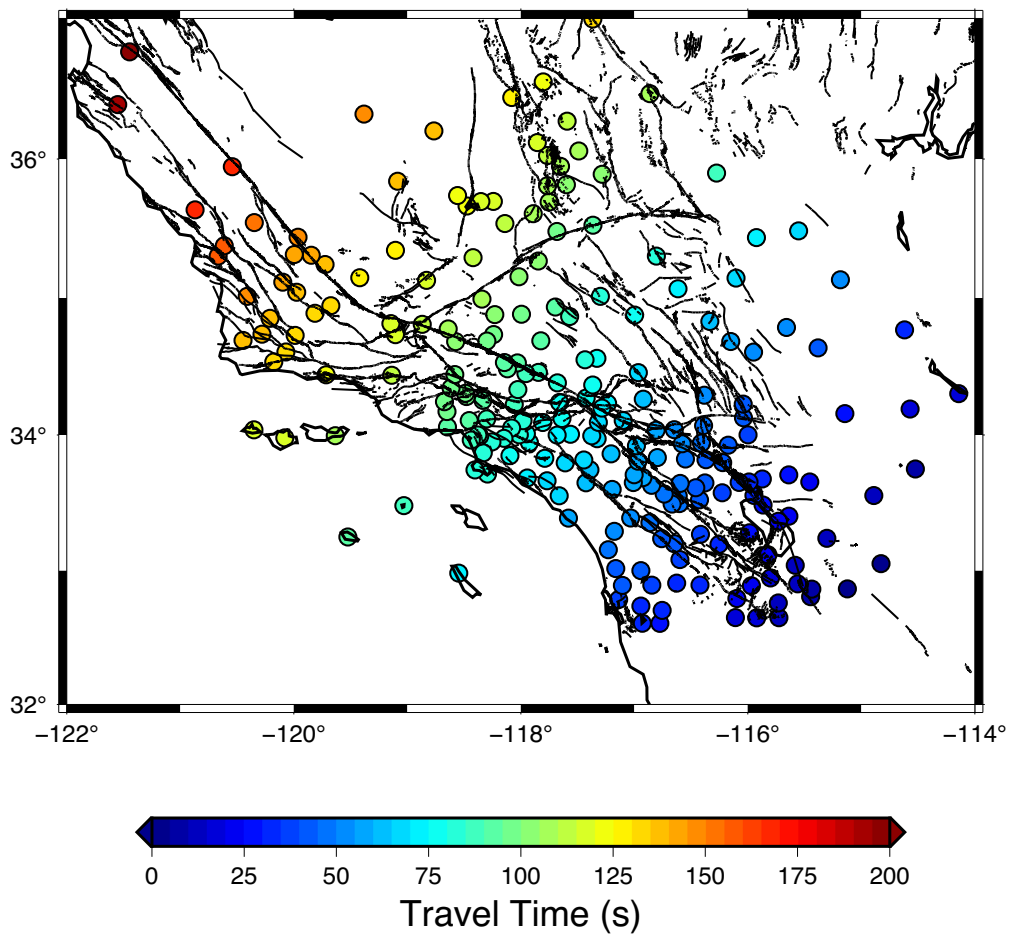
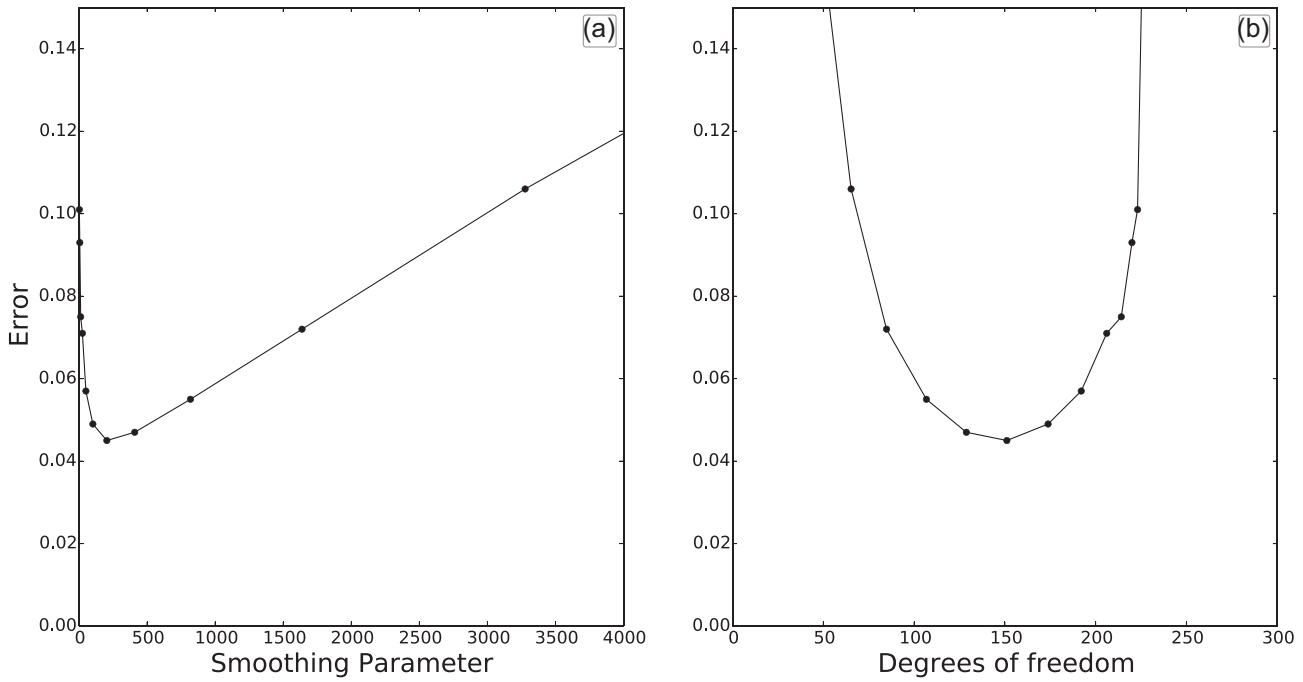
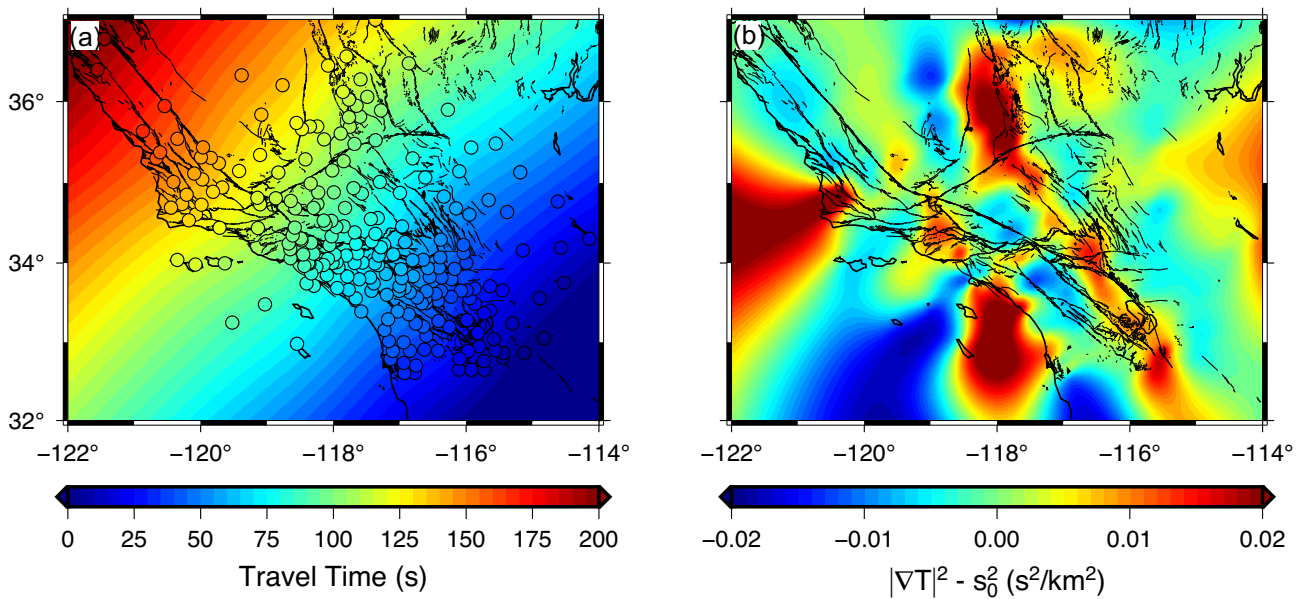


Figure 5. (a) Traveltime measurements (coloured circles) made on the vertical component Rayleigh waves from the 01/02/2019 Mexico event (Fig. 2) filtered at 25 s.



**Figure 6.** GCV error as a function of (a) smoothing parameter and (b) degrees of freedom.



**Figure 7.** (a) Traveltime measurements (coloured circles) and interpolated traveltime surface for the vertical component Rayleigh waves of the 01/02/2019 Mexico event (Fig. 2) filtered at 25 s. (b) Squared norm of the traveltime gradient (in  $s^2 km^{-2}$ ). The average squared slowness has been removed in order to enhance spatial heterogeneities. These maps were obtained using  $\lambda^* = 260$ , the optimal value of the smoothing parameter given by the GCV.

#### 4 RECONSTRUCTION OF THE PHASE FIELD WITH SMOOTHING SPLINES

In this section, we describe how the cleaned and unwrapped phase measurements can be used to reconstruct the phase field and to map phase velocities.

##### 4.1 Principle of the method

Let us consider a set of  $N$  phase measurements  $\hat{\mathbf{T}}$  obtained at the stations of our regional array. We want to reconstruct a smooth phase

field inside a regional domain on the sphere that fits these phase measurements. The phase field  $\mathbf{T}$  to reconstruct is discretized with a sampling interval  $h$  in a regular 2-D Cartesian grid, where an element  $T_i$  is the average phase inside cell  $i$ . The Cartesian grid is defined by a transverse Mercator projection, a cylindrical projection with a line of tangency of the cylinder that corresponds to the central meridian of the regional domain. Using a regular Cartesian grid allows us to use simple finite-difference approximations of the gradient and Laplacian operators. Once the phase field is reconstructed in the Cartesian grid, it is projected back to the geographic coordinates on the surface of the Earth.

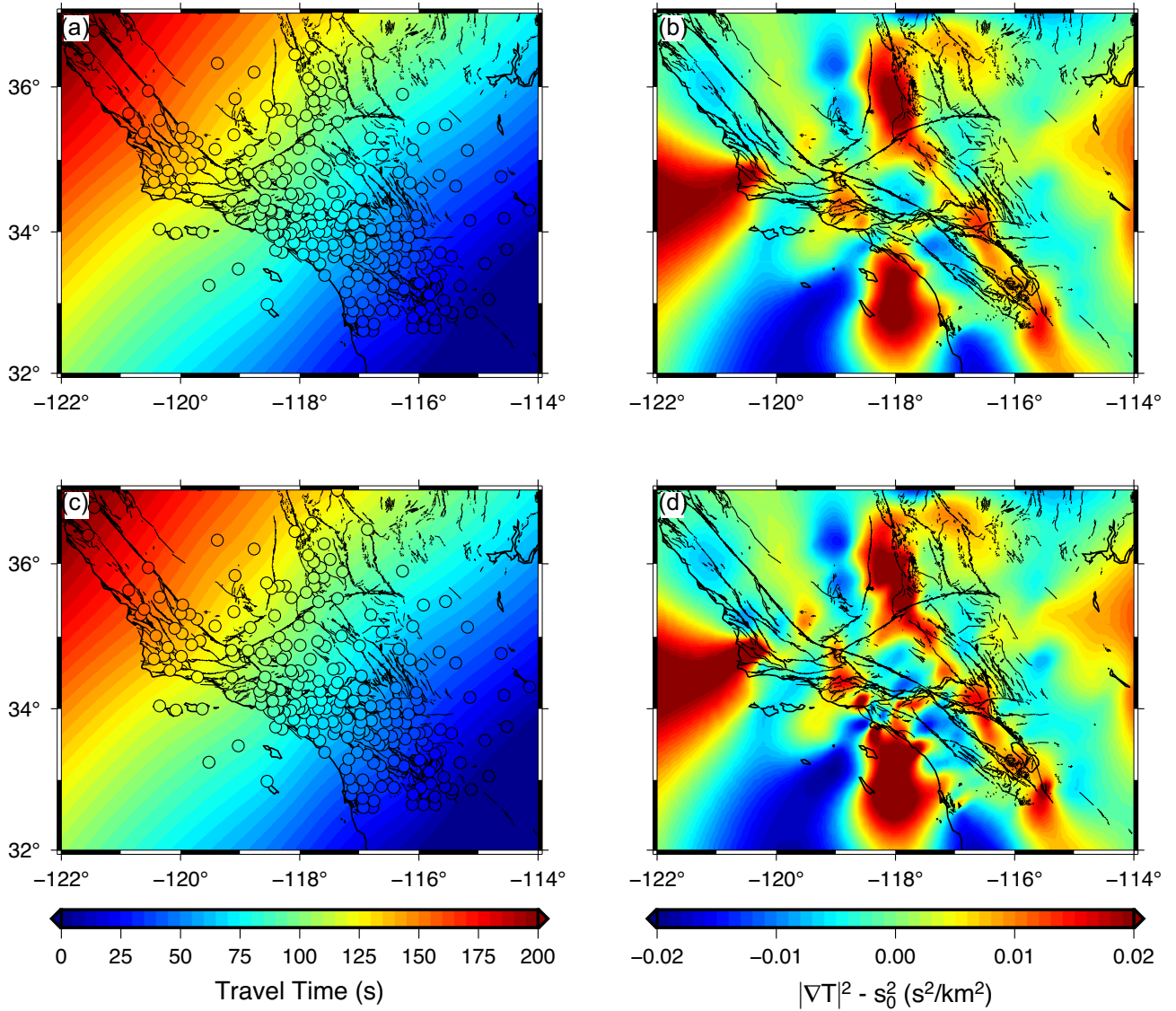


**Figure 8.** Same as Fig. 7, but for  $\lambda = 800$  (top) and  $\lambda = 50$  (bottom).

If the smoothness constraint is imposed by introducing a penalty constraint on the norm of the Laplacian of the phase, the problem can be reformulated as finding the phase field vector model  $\mathbf{T}$  that minimizes the objective function

$$\chi(\mathbf{T}) = \|\mathbf{P} \cdot \mathbf{T} - \tilde{\mathbf{T}}\|^2 + \lambda \|\mathbf{L} \cdot \mathbf{T}\|^2, \quad (3)$$

where  $\mathbf{L}$  is the discretized Laplacian operator, defined by

$$(\mathbf{L} \cdot \mathbf{T})_{i,j} = \frac{T_{i-1,j} + T_{i+1,j} + T_{i,j-1} + T_{i,j+1} - 4T_{i,j}}{h^2}, \quad (4)$$

and  $\mathbf{P}$  is the operator that samples the phase field at the station locations. In this study, we consider a bilinear interpolation operator. Because we use a fine discretization of the model with  $h = 5$  km this bilinear interpolation is sufficiently precise. For coarser grids, it may be necessary to consider a second-order Taylor series expansion as in Smith & Wessel (1990) for a better precision of the sampling operator.

The resolution of eq. (3) leads to the classical smoothing spline interpolation problem (e.g. Wahba 1990). Note that for our problem the penalty constraint on the Laplacian of the phase is justified by

the transport equation

$$2\nabla \mathbf{A} \cdot \nabla \mathbf{T} + \mathbf{A} \Delta \mathbf{T} = 0, \quad (5)$$

which in addition to the Helmholtz equation, also needs to be verified by the amplitude and phase fields (Červený 2001; Lehujeur & Chevrot 2020b). If we neglect the contribution of amplitude perturbations on the wave front, then the transport equation indeed simplifies to

$$\Delta \mathbf{T} = 0, \quad (6)$$

which is the smoothness constraint imposed in eq. (3). On the edges of the grid, the Laplacian operator is replaced by a boundary operator  $\mathbf{B}$  that imposes Neumann boundary conditions such that the gradient of the phase imposed along the normal direction is the average slowness along that direction, measured by beam forming. For example, for the left boundary, the imposed boundary condition is

$$(\mathbf{B} \cdot \mathbf{T})_{i,j} = \frac{T_{i+1,j} - T_{i,j}}{h} = s_x, \quad (7)$$

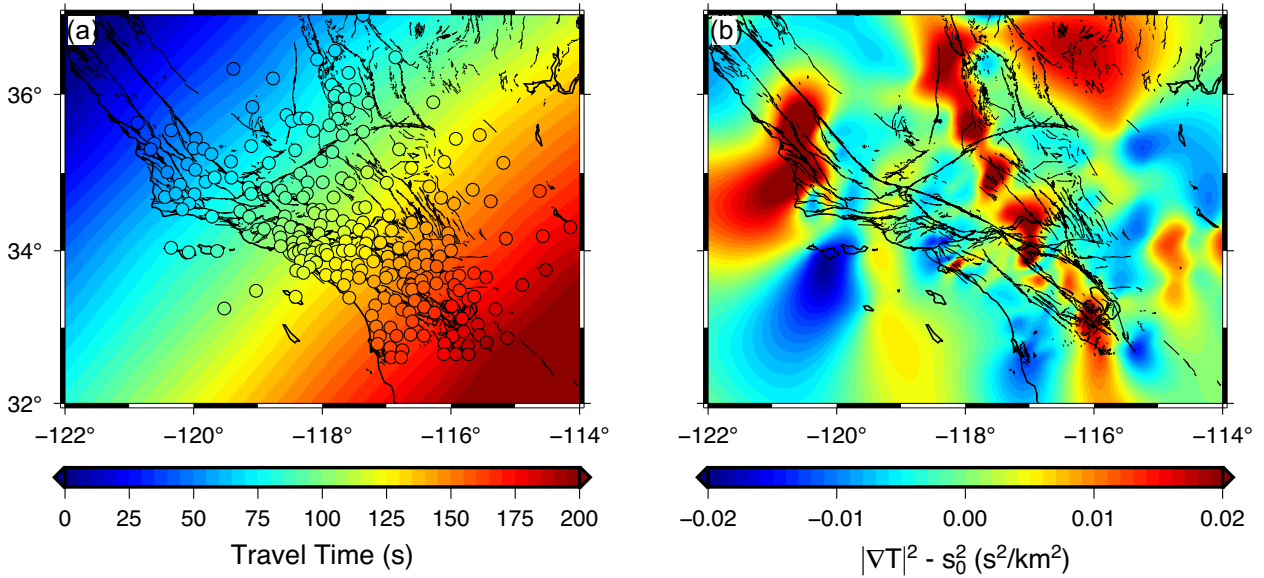


**Figure 9.** Same as Fig. 7, but for the 30/11/2018 Alaska event.

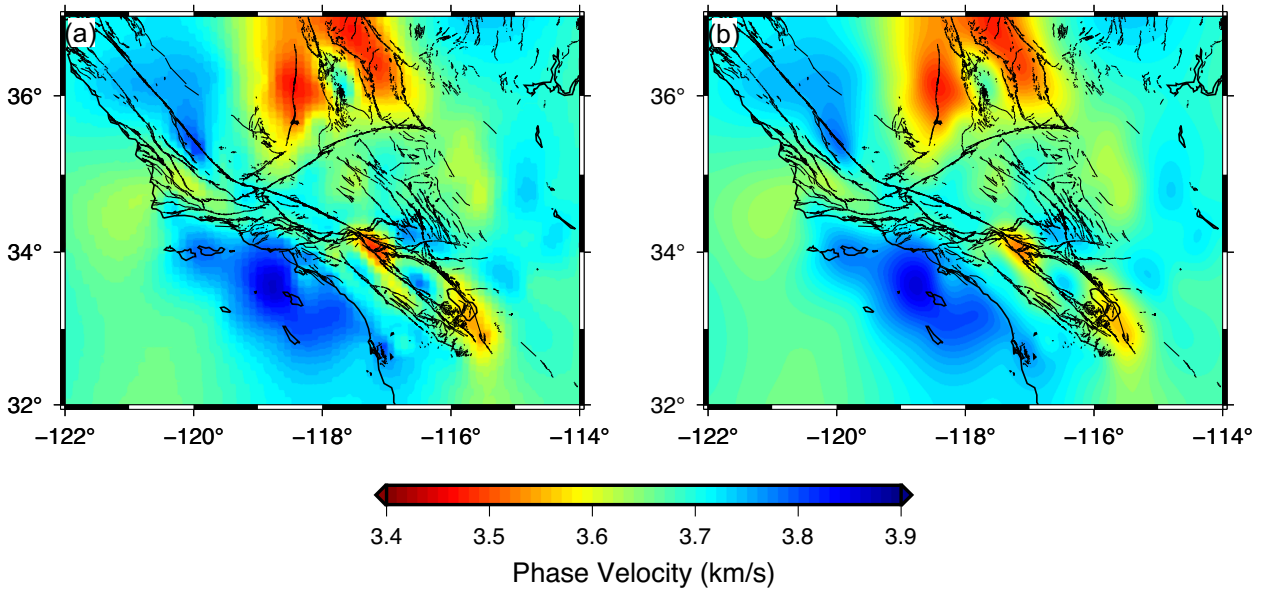


**Figure 10.** (a) Map of Rayleigh wave phase velocity at 25 s period obtained by averaging the phase velocity maps of the 27 events selected for this study. (b) Same as (a), but after applying a 45 km Gaussian filter.

where  $s_x$  is the average apparent slowness along the  $x$ -axis direction. The boundary conditions constrain the traveltimes surface outside the array to remain close to the average plane defined by the main beam given by the beamforming analysis. To summarize, our phase interpolation method can be seen as a smoothing spline interpolation problem that uses a simplified form of the wave equation as a constraint to regularize the solution both inside the regional domain and on its edges. Note that this algorithm can be easily adapted to the spherical case (see Appendix B).

For a given smoothing parameter  $\lambda$  the solution of eq. (3) is given by

$$\mathbf{T} = [\mathbf{P}^T \mathbf{P} + \lambda \mathbf{L}^T \mathbf{L}]^{-1} \mathbf{P}^T \tilde{\mathbf{T}}. \quad (8)$$

The minimization of eq. (3) searches for a compromise between close fit of the data and smoothness of the solution, that is controlled

by the smoothing parameter  $\lambda$ . If  $\lambda$  tends to 0,  $\mathbf{T}$  can be any field that exactly fits the data, whereas when  $\lambda = \infty$  the solution is the plane (curvature = 0) that minimizes the least-squares misfit with the observations.

Many different methods have been proposed to determine the optimal value of  $\lambda$ , and this problem is still an active area of research. A good overview can be found for example in Hastie *et al.* (2017). The simplest approach is to assume that the error on phase measurements  $\sigma_T$  is known and to select the smoothing parameter so that the residual time misfit equals  $N\sigma_T$ . Even if  $\sigma_T$  is often not known precisely, it can be tuned by visually inspecting the final phase velocity maps. This approach allowed us to obtain finely resolved maps of Rayleigh wave phase velocity for continental China, for periods ranging from 25 to 150 s (Zhou *et al.* 2021). Note that the popular L-curve approach (e.g.

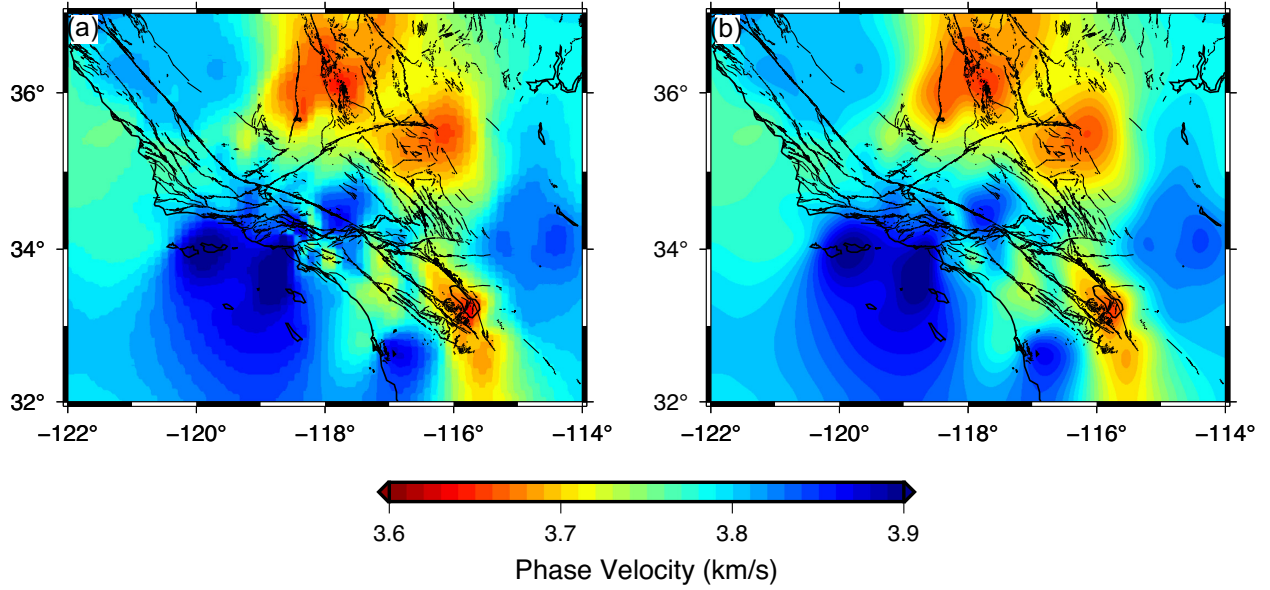


**Figure 11.** (A) Map of Rayleigh wave phase velocity at 33 s period obtained by averaging the phase velocity maps of 36 events selected for this study. (b) Same as (a), but after applying a 60 km Gaussian filter.

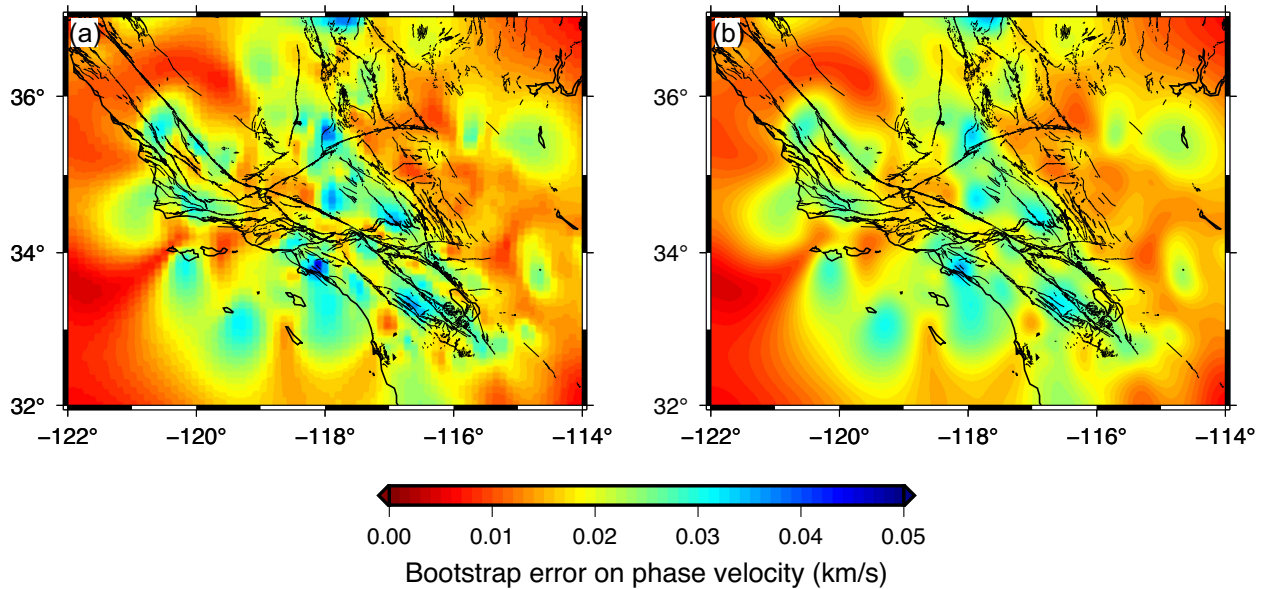


**Figure 12.** (a) Error in the 25 s phase velocity map estimated by bootstrap analysis. (b) Same as (a), but at 33 s period.

Hansen 1992), which is often used in tomographic inverse problems, does not work in the case of smoothing splines. Indeed, the curve obtained by plotting data misfits with respect to the norm of the Laplacian does not show a simple and clear kink, a behaviour attributed to the rapid decay of the singular values of the operator (e.g. Vogel 1996).

Here, we use the generalized cross-validation (GCV) method to determine the optimal smoothing parameter Golub *et al.* (1979). This method, which has recently gained in popularity as it is often used for training neural networks in deep learning applications (e.g. Goodfellow *et al.* 2016), can be applied to a wide range of problems, in particular when the L-curve approach does not converge.

Let us define  $\hat{\mathbf{T}} = \mathbf{P} \cdot \mathbf{T}$  the vector containing the predicted values of the time field at the positions of the stations. This vector is given by

$$\hat{\mathbf{T}} = \mathbf{P}(\mathbf{P}^T \mathbf{P} + \lambda \mathbf{L}^T \mathbf{L})^{-1} \mathbf{P}^T \tilde{\mathbf{T}} \quad (9)$$

$$= \mathbf{S} \tilde{\mathbf{T}}, \quad (10)$$

where  $\mathbf{S}$  is a symmetric, positive definite matrix, often referred to as the influence (Wahba 1990) or smoother (Hastie *et al.* 2017) matrix. The effective degrees of freedom of a smoothing spline (Hastie *et al.* 2017) is defined as the sum of the diagonal elements of  $\mathbf{S}$ :

$$df_\lambda = \text{trace}(\mathbf{S}). \quad (11)$$

The GCV method approximates the prediction error by Wahba (1990) and Hastie *et al.* (2017)

$$\text{Error}_{\text{gcvd}} = \frac{1}{N} \sum_{i=1}^N \left( \frac{\hat{T}_i - \tilde{T}_i}{1 - \text{trace}(\mathbf{S})/N} \right)^2. \quad (12)$$

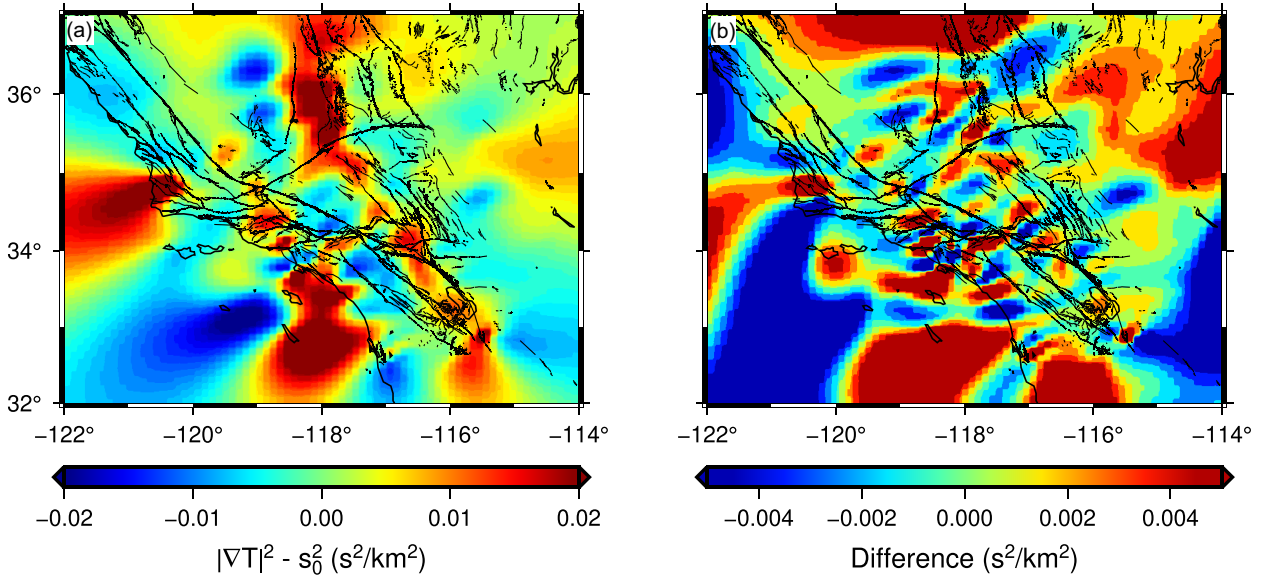


**Figure 13.** (a) Same as Fig. 7(b) after interpolation performed with splines in tension. (b) Difference between (a) and the squared norm traveltime gradient shown in Fig. 7(b).

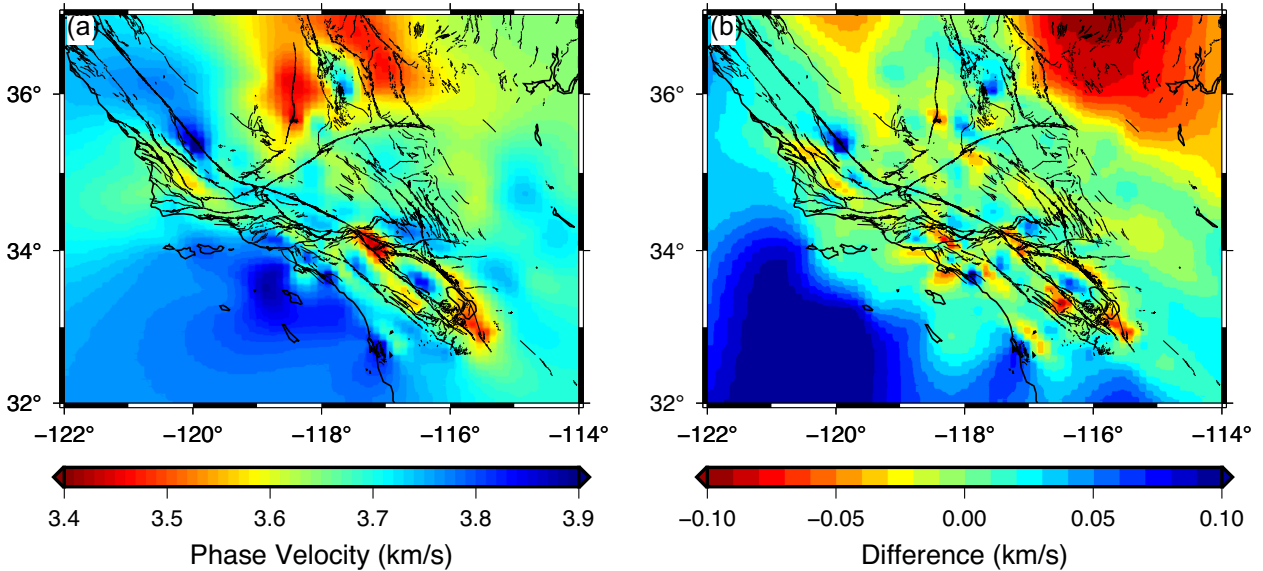


**Figure 14.** (a) Same as Fig. 10 but for interpolations performed with splines in tension. (b) Difference between the phase velocity map (a) and the phase velocity map shown in Fig. 10 obtained with smoothing splines.

The derivation of eq. (12) is detailed in Appendix A. The main advantage of GCV is that the computation of the trace of  $S$  can be computed for a fraction of the cost compared to its elements. To compute the trace of  $S$  we follow the stochastic approach of Hutchinson (1989), which only involves the resolution of a linear system of equation similar to eq. (3). This algorithm can thus be used to solve smoothing problems with a very large number of parameters.

Fig. 6(a) shows the GCV error as a function of the smoothing parameter for the interpolation of the traveltime measurements shown in Fig. 5. Fig. 6(b) shows the same errors but this time as a function of the number of degrees of freedom. Fig. 7(a) shows the interpolated traveltime surface obtained by using  $\lambda^* = 260$ , the smoothing parameter that minimizes the prediction error. The wave

front distortions observed in the traveltime measurements are accurately fitted in the traveltime map. Outside the seismic network, the traveltime surface is more regular. It smoothly connects to the mesh boundaries, where the phase gradient is again the slowness of the average coherent beam. Fig. 7(b) shows the squared norm of the gradient of the traveltime surface shown in Fig. 7(a). Not surprisingly, the spatial derivation has the effect of strongly boosting the small-scale irregularities of the traveltime surface.

Fig. 8 shows the traveltime surfaces obtained with  $\lambda = 800$  (top) and  $\lambda = 50$  (bottom), that is, when respectively multiplying or dividing the optimal smoothing parameter by 4. The reconstructed traveltime surfaces are almost indistinguishable. Whereas notable differences are observed in the gradient maps the main anomaly patterns are also quite similar, which suggests that the choice of the

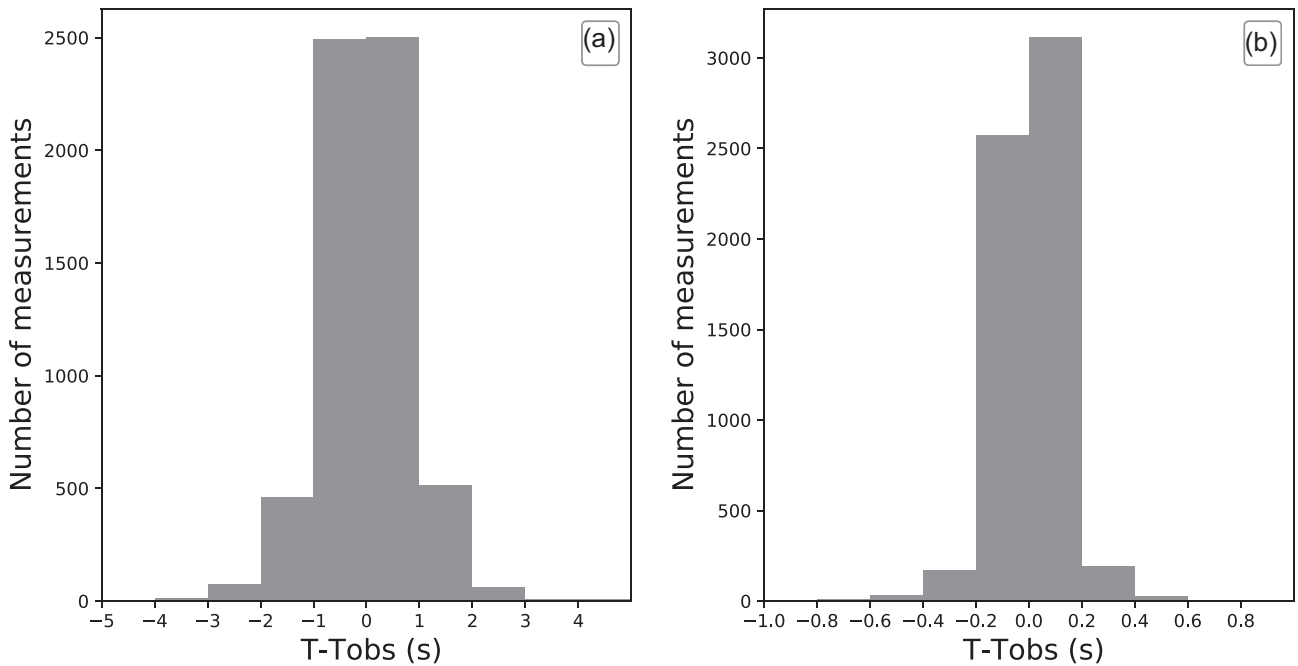


**Figure 15.** (a) Histogram of traveltime residuals with respect to the average plane waves at 25 s period. (b) Histogram of traveltime deviations with respect to the traveltime surfaces reconstructed with smoothing splines.

smoothing parameter is not critical, provided it is not too far (within an order of magnitude) from the optimal value.

Fig. 9 shows the traveltime surface and its gradient for the 2018 November 30 Alaska event. The traveltime gradients for the Alaska and Mexico events show strong differences even though the two wave fronts propagate along opposite directions. In that particular case, the apparent phase velocities should be the same with no contribution from azimuthal anisotropy. The strong deviations observed in the gradient maps thus demonstrate the strong imprint of scattering effects and/or noise in the traveltime measurements on individual traveltime gradient maps, and consequently also on individual phase velocity maps.

## 5 AVERAGE PHASE VELOCITY MAPS

In the time period considered (2017–2020), we have selected 27 and 35 events at, respectively, 25 and 33 s period which were all processed following the method described in the previous section. Overall, the azimuthal distribution of source regions (Fig. 1) is uneven but sufficiently variable to keep the contribution of any azimuthal anisotropy small. Not surprisingly, a predominant number of wave fronts come from the Tonga region. Earthquakes in Alaska and Aleutian Islands are also well represented, as well as earthquakes in Mexico and South America (Colombia, Peru and Chile). The final phase velocity map at 25 s (Fig. 10a) was obtained by averaging the 27 phase velocity maps resulting from the analysis of each individual wave front. Bootstrap analysis led to very similar results. We also obtained very similar phase velocity maps if we first averaged the maps in  $10^\circ$  backazimuth windows and then computed the average of these averages backazimuth maps. These results thus seem to suggest that even though the azimuthal coverage is uneven, the azimuthal distribution of teleseismic sources is sufficient to get robust isotropic phase velocity maps for Southern California. We also observed that phase velocities converge to very stable values

once  $\sim 20$  phase velocity maps are averaged. A movie showing the behaviour of the averaging process as a function of the number of wave fronts averaged is included in the Supporting Information. When a small number of phase velocity maps ( $< 10$ ) are averaged, the phase velocity map shows significant artefacts produced by scattering effects. These artefacts progressively disappear and coherent patterns in the lateral variations of phase velocity start to emerge and get more and more stable. Fig. 10(b) shows the final velocity map filtered with a 45 km 2-D Gaussian filter. This filter removes any remaining artefacts at scales shorter than half the wavelength of the Rayleigh wave (Lehjeur & Chevrot 2020b). The initial and filtered phase velocity maps being extremely similar, these artefacts must be quite small. With this approach, we were able to obtain robust and stable phase velocity maps from 25 to 150 s, that will be presented in more details in a future contribution. Figs 11(a) and (b) show the same maps as in Figs 10(a) and (b), but for a period of 33 s.

We also estimated the errors in the phase velocity maps with a bootstrap analysis (Fig. 12). Slightly larger errors are observed at 25 s but overall, the errors are everywhere small and at least 10 times smaller than the lateral variations seen in the average phase velocity maps.

## 6 DISCUSSION

### 6.1 Smoothing splines versus splines in tension

As already stated in the introduction, the main difference between splines in tension and smoothing splines is that the former impose a perfect match with the measurements whereas the latter relax this constraint to provide a smoother interpolated solution. For this reason, splines in tension will lead to more oscillating solutions where the observation points are very close to each other or where the separation between observation points is highly variable. This

is typically the case for a regional seismic network, and for the Southern California Seismic Network in particular, which has a very high density of stations in the Los Angeles area, and a much sparser distribution of stations in the Central Valley or in the Mojave desert, for example.

The norm of the gradient of the traveltimes surface reconstructed with splines in tension for the Mexico event (Fig. 13a) is very similar to the gradient obtained with smoothing splines (Fig. 7b), but it is clearly more oscillatory, as can be seen in Fig. 13(b) which shows the difference between the two gradients. The average phase velocity map obtained by averaging all the traveltimes surfaces reconstructed with splines in tension (Fig. 14a) is in excellent agreement with the average phase velocity map obtained with smoothing splines (Fig. 10). The differences between the two phase velocity maps (Fig. 14b) are strong outside the seismic network, which suggests that in that part of the model, the reconstructed phase velocity anomalies are not robust and are mostly controlled by the interpolation scheme and the boundary conditions. Inside the seismic network, the differences are much smaller and the small-scale artefacts present in the model obtained with splines in tension are always within the errors of the model obtained with smoothing splines (Fig. 12). These errors could be easily attenuated by applying an additional smoothing filter, albeit with a slight degradation of the spatial resolution.

To summarize, the results of eikonal tomography performed with splines in tension and smoothing splines are very similar, but smoothing splines seem to provide a slightly better spatial resolution and smaller artefacts.

## 6.2 Traveltimes misfits

We now estimate the *a priori* and *a posteriori* traveltimes misfits by comparing the observations with our phase measurements with the traveltimes surfaces corresponding to the average plane waves and to the wave fronts reconstructed by smoothing spline interpolation. Fig. 15(a) shows the distribution of the traveltimes deviations with respect to the average plane waves at 25 s period, combining the measurements from all the events in the data set. These traveltimes misfits follow a normal distribution with a standard deviation of 0.84 s. At 33 s period, we observe a very similar distribution with a slightly larger standard deviation of 1.04 s. The deviations from the traveltimes surfaces obtained with smoothing splines shown in Fig. 15(b) are one order of magnitude smaller, with a standard deviation of 0.11 s at 25 s period, and 0.15 s at 33 s period. In the future, we may thus simply select the smoothing parameter  $\lambda$  that leads to traveltimes misfits compatible with these estimates.

It is important to note that the final traveltimes misfits only quantify the goodness of fit and should not be interpreted in terms of measurement error. Indeed, traveltimes surfaces reconstructed by smoothing splines are still contaminated by the effects of clock errors, scattering, seismic anisotropy, multipathing, or interference with overtones. Quantifying the contribution of each source of error is a difficult problem that is clearly beyond the scope of this study. For example, the effect of interference between the fundamental mode and overtones has been studied by Hariharan *et al.* (2022) by analysing synthetic seismograms computed by normal mode summations. They found that the interference between the fundamental mode of Rayleigh waves with the overtones is particularly strong at epicentral distances shorter than  $25^\circ$  and larger than  $120^\circ$ , and that the focal mechanism can also affect significantly the strength of the interference. The effects of scattering and seismic anisotropy

could also be quantified by 3-D modelling of surface waves, but this would require a detailed knowledge of the isotropic and anisotropic structure of the lithosphere which remains elusive, especially at short scales.

## 6.3 Comparison with previous tomographic studies

The phase velocity maps shown in Figs 10 and 11 are overall in excellent agreement with the results obtained with classical finite-frequency tomographic methods (Yang & Forsyth 2006; Prindle & Tanimoto 2006; Lee *et al.* 2014). In all these models, pronounced low velocity anomalies are observed beneath the southern Sierra Nevada and Salton Trough and a strong high velocity anomaly in the offshore borderland region. However, our phase velocity maps obtained with eikonal tomography seem to reveal the structures with much finer details. Whereas characterizing resolution analysis of eikonal tomography is beyond the scope of this study, we note that many small-scale features in our phase velocity map at 25 s period can be associated to well known structures in the Southern California crust. For example, the low velocity anomalies beneath the eastern Transverse Ranges and southern Sierra Nevada have been documented as regions where the Moho is deeper (35–38 km) than average from the analysis of receiver functions (Zhu & Kanamori 2000; Yan & Clayton 2007). Beneath the Great Valley, we observe a westward increase of phase velocity, which would suggest an eastward dip of the Moho, in rather good agreement with the results of refraction profiles (Holbrook & Mooney 1987). The other salient feature is the pronounced low velocity anomaly to the southeast of the Salton Trough. Heat flow in the Salton Trough is very high, of the order of  $140 \text{ mW m}^{-2}$  (Lachenbruch *et al.* 1985). Such a value suggests that the crust directly lies above the asthenosphere (Lachenbruch *et al.* 1985; van Wijk *et al.* 2019). Wide-angle reflection profiles have evidenced a  $\sim 10$  km thick accumulation of sediments in the Salton Trough, and a strong reflector at  $\sim 20$  km depth, which has been interpreted as the Moho (Han *et al.* 2016). Whereas some controversies remain regarding the nature of the hyper-extended Salton Trough crust (Han *et al.* 2016; van Wijk *et al.* 2019), the very low velocities observed to the south of the Salton Trough are consistent with the active rifting processes that take place in that region.

## 6.4 Perspectives for Helmholtz tomography

Whereas eikonal tomography provides robust isotropic phase velocity maps, exploiting the amplitude information should allow us to remove artefacts produced by scattering effects. We can thus expect that with Helmholtz tomography the convergence will be faster even though the final isotropic model will not differ significantly from the one obtained with eikonal tomography if the number of exploitable wave fronts is sufficient. It may thus be beneficial to move from eikonal to Helmholtz tomography for tomographic applications on dense regional arrays deployed during a short period of time and which have recorded a limited number of large teleseismic events. As demonstrated by Lin & Ritzwoller (2011), the other advantage of Helmholtz tomography is that because it provides individual phase velocity maps free of scattering artefacts (without averaging), it is then possible to constrain the variations of velocities as a function of the propagation direction of the wave front, that is, to constrain azimuthal anisotropy. Therefore, there is a clear interest to extend the present work to exploit the amplitude information. We will present how our smoothing spline approach can be generalized to

Helmholtz tomography in a future contribution. Because Helmholtz tomography involves computing the Laplacian (i.e. second spatial derivatives) of the amplitude field, we thus expect important benefits coming from the utilization of smoothing splines for this imaging approach.

## 7 CONCLUSIONS

We have developed a new smoothing spline approach to interpolate the traveltime of fundamental-mode Rayleigh wave fronts crossing dense regional arrays. The gradients of the reconstructed travel-time surfaces directly provide phase velocity maps without having to resolve a large tomographic inverse problem. Instead, eikonal tomography only involves resolving a small smoothing spline interpolation problem for each selected wave front. This approach is thus both simpler to implement and more efficient than classical tomographic approaches. But its main advantage is that the final model is obtained by a simple averaging process, without imposing any additional regularization or smoothing constraints that invariably lead to a degradation of resolution.

Using Rayleigh waves from a selection of recent earthquakes recorded by the Southern California Seismic Network, we obtained phase velocity maps at 25 and 33 s period. These maps are in overall excellent agreement with the results of previous tomographic studies performed in that region. The most salient features in these maps are the pronounced low velocity anomalies beneath the southern Sierra Nevada and the southern part of the Salton Trough, and a high velocity anomaly beneath the Great Valley and the offshore borderland region.

In eikonal tomography, the most critical and time consuming task is the data selection, whereas the fundamental-mode extraction and beamforming to determine the average azimuth and slowness of the wave front can be fully automatized. We found that below 25 s period, the S/N quickly decreases and multipathing effects become predominant. As a consequence, phase measurements become extremely challenging with surface waves generated by earthquakes. However, as demonstrated by Shapiro *et al.* (2005) in their pioneering tomographic study of southern California, and later confirmed by numerous other studies (e.g. Zigone *et al.* 2014; Barak *et al.* 2015; Wang *et al.* 2020), dispersion measurements can be obtained in the period range 3–20 s by correlating ambient seismic noise at different pairs of stations. The exploitation of ambient seismic noise is thus a useful backup in order to extend regional eikonal surface wave tomography toward shorter periods (e.g. Jiang *et al.* 2018).

## ACKNOWLEDGMENTS

We thank an anonymous reviewer and Wolfgang Friederich for constructive and insightful comments that helped to improve the manuscript. This work was supported by OROGEN, a tripartite research project between the CNRS, Total and BRGM, and by the ANR AAPG program (project CLEARVIEW, ANR-17-CE23-0022).

## DATA AVAILABILITY

The seismic data from the Southern California Seismic Network used in this study are available at IRIS (<https://www.iris.edu/hq/>).

## REFERENCES

- Aki, K., Christofferson, A. & Husebye, E.S., 1977. Determination of the three-dimensional seismic structures of the lithosphere, *J. geophys. Res.*, **82**, 277–296.
- Barak, S., Klemperer, S.L. & Lawrence, J.F., 2015. San Andreas Fault dip, Peninsular Ranges mafic lower crust and partial melt in the Salton Trough, Southern California, from ambient-noise tomography, *Geochem. Geophys. Geosyst.*, **16**, 3946–3972.
- Bodin, T. & Maupin, V., 2008. Resolution potential of surface wave phase velocity measurements at small arrays, *Geophys. J. Int.*, **172**, 698–706.
- Capon, J., 1969. High-resolution frequency-wavenumber spectrum analysis, *Proc. IEEE*, **57**, 1408–1419.
- Chevrot, S. & Zhao, L., 2007. Multi-scale finite-frequency Rayleigh wave tomography of the Kaapvaal craton, *Geophys. J. Int.*, **169**, 201–215.
- Friederich, W. & Wielandt, E., 1995. Interpretation of seismic surface waves in regional networks: joint estimation of wavefield geometry and local phase velocity. Method and numerical tests, *Geophys. J. Int.*, **120**, 731–744.
- Friederich, W., Wielandt, E. & Stange, S., 1994. Non-plane geometry of seismic surface wavefields and their implications for regional surface-wave tomography, *Geophys. J. Int.*, **119**, 931–948.
- Golub, G.H., Heath, M. & Wahba, G., 1979. Generalized cross-validation as a method for choosing a good ridge parameter, *Technometrics*, **21**(2), 215–223.
- Goodfellow, I., Bengio, Y. & Courville, A., 2016. *Deep Learning*, the MIT Press, Cambridge, MA, USA.
- Han, L. *et al.*, 2016. Continental rupture and the creation of new crust in the Salton Trough rift, Southern California and northern Mexico: Results from the Salton Seismic Imaging Project, *J. geophys. Res.: Solid Earth*, **121**(10), 7469–7489.
- Hansen, P.C., 1992. Analysis of discrete ill-posed problems by means of the L-curve, *SIAM Rev.*, **34**, 561–580.
- Hariharan, A., Dalton, C.A., Ma, Z. & Ekström, G., 2020. Evidence of overtone interference in fundamental-mode Rayleigh wave phase and amplitude measurements, *J. geophys. Res.: Solid Earth*, **125**(1), doi:10.1029/2019jb018540.
- Hariharan, A., Dalton, C.A., Babikoff, J. & Ekström, G., 2022. Controls on surface wave overtone interference, *Geophys. J. Int.*, **228**(3), 1665–1683.
- Hastie, T., Tibshirani, R. & Friedman, J., 2017. *The Elements of Statistical Learning*, 2nd edn, Springer.
- Holbrook, W. & Mooney, W.D., 1987. The crustal structure of the axis of the Great Valley, California, from seismic refraction measurements, *Tectonophysics*, **140**(1), 49–63.
- Hutchinson, M., 1989. A stochastic estimator of the trace of the influence matrix for laplacian smoothing splines, *Commun. Stat.—Simulat. Comput.*, **18**(3), 1059–1076.
- Jiang, C., Schmandt, B., Hansen, S.M., Dougherty, S.L., Clayton, R.W., Farrell, J. & Lin, F.-C., 2018. Rayleigh and S wave tomography constraints on subduction termination and lithospheric foundering in central California, *Earth planet. Sci. Lett.*, **488**, 14–26.
- Jin, G. & Gaherty, J.B., 2015. Surface wave phase-velocity tomography based on multichannel cross-correlation, *Geophys. J. Int.*, **201**, 1383–1398.
- Kolínský, P., Schneider, F.M. & Bokelmann, G., 2020. Surface wave diffraction pattern recorded on AlpArray: Cameroon volcanic line case study, *J. geophys. Res.: Solid Earth*, **125**(7), doi:10.1029/2019jb019102.
- Lachenbruch, A.H., Sass, J.H. & Galanis, S.P., 1985. Heat-flow in southernmost California and the origin of the Salton Trough, *J. geophys. Res.*, **90**, 6709–6736.
- Lee, E.-J., Chen, P., Jordan, T.H., Maechling, P.B., Denolle, M. A.M. & Beroza, G.C., 2014. Full-3-D tomography for crustal structure in Southern California based on the scattering-integral and the adjoint-wavefield methods, *J. geophys. Res.: Solid Earth*, **119**(8), 6421–6451.
- Lehujeur, M. & Chevrot, S., 2020a. Eikonal tomography using coherent surface waves extracted from ambient noise by iterative matched filtering

- Application to the large-N Maupasacq array, *J. geophys. Res.*, **125**, e2020JB019363, doi:10.1029/2020JB019363.
- Lehujeur, M. & Chevrot, S., 2020b. On the validity of the eikonal equation for surface-wave phase-velocity tomography, *Geophys. J. Int.*, **223**, 908–914.
- Levshin, A.L. & Ritzwoller, M.H., 2001. Automated detection, extraction, and measurement of regional surface waves, *Pure appl. Geophys.*, **158**, 1531–1545.
- Lin, F.C. & Ritzwoller, M.H., 2011. Helmholtz surface wave tomography for isotropic and azimuthally anisotropic structure, *Geophys. J. Int.*, **186**, 1104–1120.
- Lin, F.C., Ritzwoller, M.H. & Snieder, R., 2009. Eikonal tomography: surface wave tomography by phase front tracking across a regional broad-band seismic array, *Geophys. J. Int.*, **177**, 1091–1110.
- Liu, Y. & Holt, W.E., 2015. Wave gradiometry and its link with Helmholtz equation solutions applied to USArray in the eastern U.S., *J. geophys. Res.*, **120**, doi:10.1002/2015JB011982.
- Pollitz, F.F., 2008. Observations and interpretation of fundamental mode Rayleigh wavefields recorded by the Transportable Array (USArray), *J. geophys. Res.*, **113**, doi:10.1029/2007JB005556.
- Pollitz, F.F. & Snoko, J.A., 2010. Rayleigh-wave phase velocity maps and three-dimensional shear velocity structure of the western US from local non-plane surface wave geometry, *Geophys. J. Int.*, **180**, 1153–1169.
- Prindle, K. & Tanimoto, T., 2006. Teleseismic surface wave study for S-wave velocity structure under an array: Southern California, *Geophys. J. Int.*, **166**, 601–621.
- Qiu, H., Lin, F.-C. & Ben-Zion, Y., 2019. Eikonal tomography of the Southern California Plate Boundary Region, *J. geophys. Res.: Solid Earth*, **124**(9), 9755–9779.
- Shapiro, N.M., Campillo, M., Stehly, L. & Ritzwoller, M.H., 2005. High-resolution surface-wave tomography from ambient seismic noise, *Science*, **307**, 1615–1618.
- Smith, W. H.F. & Wessel, P., 1990. Gridding with continuous curvature splines in tension, *Geophysics*, **55**(3), 293–305.
- Tanimoto, T., 1990. Modelling curved surface wave paths: membrane surface wave synthetics, *Geophys. J. Int.*, **102**(1), 89–100.
- Tromp, J. & Dahlen, F.A., 1993. Variational principles for surface wave propagation on a laterally heterogeneous Earth-III. Potential representation, *Geophys. J. Int.*, **112**(2), 195–209.
- Červený, V., 2001. *Seismic Ray Theory*, Cambridge University Press.
- van Wijk, J.W., Heyman, S.P., Axen, G.J. & Persaud, P., 2019. Nature of the crust in the northern Gulf of California and Salton Trough, *Geosphere*, **15**(5), 1598–1616.
- Vogel, C.R., 1996. Non-convergence of the L-curve regularization parameter selection method, *Inverse Probl.*, **12**, 535–547.
- Wahba, G., 1990. *Spline Models for Observational Data*, SIAM.
- Wang, K., Jiang, C., Yang, Y., Schulte-Pelkum, V. & Liu, Q., 2020. Crustal deformation in Southern California constrained by radial anisotropy from ambient noise adjoint tomography, *Geophys. Res. Lett.*, **47**(12), doi:10.1029/2020gl088580.
- Wessel, P. & Bercovici, D., 1998. Interpolation with splines in tension: a Green's function approach, *Math. Geol.*, **30**(1), 77–93.
- Wielandt, E., 1993. Propagation and structural interpretation of non-plane waves, *Geophys. J. Int.*, **113**, 45–53.
- Yan, Z. & Clayton, R.W., 2007. Regional mapping of the crustal structure in southern California from receiver functions, *J. geophys. Res.*, **112**(B5), doi:10.1029/2006jb004622.
- Yang, Y. & Forsyth, D.W., 2006. Rayleigh wave phase velocities, small-scale convection, and azimuthal anisotropy beneath southern California, *J. geophys. Res.*, **111**, B07306.
- Zhou, W., Chevrot, S., Lehujeur, M., Zhao, L. & Xia, S., 2021. Eikonal surface-wave tomography of continental China, *Geophys. J. Int.*, Submitted, 2022.
- Zhu, L.P. & Kanamori, H., 2000. Moho depth variation in southern California from teleseismic receiver functions, *J. geophys. Res.*, **105**, 2969–2980.

- Zigone, D., Ben-Zion, Y., Campillo, M. & Roux, P., 2014. Seismic tomography of the Southern California plate boundary region from noise-based Rayleigh and Love waves, *Pure appl. Geophys.*, **172**(5), 1007–1032, doi:10.1007/s00024-014-0872-1.

## SUPPORTING INFORMATION

Supplementary data are available at *GJI* online.

### suppl\_data

Please note: Oxford University Press is not responsible for the content or functionality of any supporting materials supplied by the authors. Any queries (other than missing material) should be directed to the corresponding author for the paper.

## APPENDIX A: PRINCIPLE OF GENERALIZED CROSS-VALIDATION

The principle of the cross-validation method is to estimate the error on an independent data set that is not used in the inversion (Hastie *et al.* 2017). In the  $K$ -fold cross-validation, the data are split into approximately  $K$  equal parts. For each part, a model is obtained by fitting the  $(K - 1)$  other parts, and the error is estimated from

$$\text{Error}_{cvd} = \frac{1}{N} \sum_{i=1}^N \left( \hat{T}_i^{-\kappa(i)} - \tilde{T}_i \right)^2, \quad (\text{A1})$$

where  $\hat{T}_i^{-\kappa(i)}$  is the phase model obtained with the  $\kappa(i)$ th part of the data removed. If  $K = N$ , then

$$\text{Error}_{cvd} = \frac{1}{N} \sum_{i=1}^N \left( \hat{T}_i^{-i} - \tilde{T}_i \right)^2, \quad (\text{A2})$$

where  $\hat{T}_i = (\mathbf{P} \cdot \mathbf{T})_i = \mathbf{P}_i \cdot \mathbf{T}$  is the phase model reconstructed from the data set and  $\hat{T}_i^{-i}$  is the same quantity obtained by dropping the  $i$ th station from the data set. The projector operator  $\mathbf{P}_i$  samples the phase field at the position of station  $i$ .

Let us define the vector

$$\tilde{\mathbf{T}}^{-i} = \tilde{\mathbf{T}} + \mathbf{P}_i(\hat{\mathbf{T}}^{-i} - \tilde{\mathbf{T}}) \quad (\text{A3})$$

where the  $i$ th data  $\tilde{T}_i$  has been removed. Inserting eq. (A3) into eq. (10), we get

$$\hat{\mathbf{T}}^{-i} = \mathbf{S} \tilde{\mathbf{T}} + \mathbf{S} \mathbf{P}_i(\hat{\mathbf{T}}^{-i} - \tilde{\mathbf{T}}) \quad (\text{A4})$$

$$= \hat{\mathbf{T}} + \mathbf{S} \mathbf{P}_i(\hat{\mathbf{T}}^{-i} - \tilde{\mathbf{T}}), \quad (\text{A5})$$

and therefore

$$\hat{\mathbf{T}}^{-i} = \mathbf{P}_i \hat{\mathbf{T}}^{-i} \quad (\text{A6})$$

$$= \mathbf{P}_i \hat{\mathbf{T}} + \mathbf{P}_i \mathbf{S} \mathbf{P}_i(\hat{\mathbf{T}}^{-i} - \tilde{\mathbf{T}}) \quad (\text{A7})$$

$$= \hat{T}_i + S_{ii}(\hat{T}_i^{-i} - \tilde{T}_i). \quad (\text{A8})$$

Subtracting  $\tilde{T}_i$  from each side of eq. (A8), we finally obtain

$$(1 - S_{ii})(\hat{T}_i^{-i} - \tilde{T}_i) = \hat{T}_i - \tilde{T}_i, \quad (\text{A9})$$

which demonstrates that

$$\text{Error}_{cvd} = \frac{1}{N} \sum_{i=1}^N \left( \frac{\hat{T}_i - \tilde{T}_i}{1 - S_{ii}} \right)^2 \quad (\text{A10})$$

The GCV method assumes that  $S_{ii}$  can be approximated by  $\text{trace}(\mathbf{S})/N$ , which leads to the definition of the GCV error (12).

## APPENDIX B: EXTENSION TO SPHERICAL COORDINATES

For a surface wave propagating on the surface of a homogeneous and spherical Earth with phase velocity  $c$ , the amplitude will vary because of the geometrical expansion of the wave front according to

$$\mathbf{A}(\lambda, \varphi) = \frac{A_0}{\sqrt{2\pi R \sin D(\lambda, \varphi)}}, \quad (\text{B1})$$

where

$$D(\lambda, \varphi) = \arccos [\sin \lambda_E \sin \lambda + \cos \lambda_E \cos \lambda \cos(\varphi - \varphi_E)], \quad (\text{B2})$$

is the epicentral distance,  $\lambda$ ,  $\varphi$  the latitude and longitude,  $A_0$  a constant,  $R$  the radius of the Earth and  $\lambda_E$ ,  $\varphi_E$  the longitude and latitude of the source.

The transport equation is given by eq.(5), which we rewrite as

$$2\nabla(\log \mathbf{A}) \cdot \nabla \mathbf{T} + \Delta \mathbf{T} = 0. \quad (\text{B3})$$

In Cartesian coordinates, neglecting the amplitude variations in the direction of propagation leads to  $\Delta \mathbf{T} = 0$ , which gives the quadratic penalty term used to constraint the interpolation of the time field in eq. (3). In spherical coordinates, we cannot simply drop the amplitude term of the transport equation because geometrical effects may not be negligible especially if the studied area is large, and we thus use the new smoothing operator  $\mathbf{L} = 2\nabla(\log \mathbf{A}) \cdot \nabla + \Delta$ , where the gradient ( $\nabla$ ) and Laplacian ( $\Delta$ ) operators are expressed in spherical coordinates.